

Non-Boussinesq approach for turbulent buoyant flows in enclosure with horizontal vent and forced inlet port



R. Harish, K. Venkatasubbaiah*

Department of Mechanical and Aerospace Engineering, Indian Institute of Technology Hyderabad, Hyderabad 502205, India

ARTICLE INFO

Article history:

Received 13 October 2014

Revised 7 April 2015

Accepted 28 May 2015

Available online 11 July 2015

Keywords:

Non-Boussinesq approach

Horizontal vent

Grashof number

Forced inlet port

ABSTRACT

The effects of forced ambient velocity on thermal plume behavior in a ceiling vented square enclosure are numerically investigated. Turbulence is modeled by unsteady Favre-averaged Navier–Stokes (UFANS) equation with Lam Bremhorst low Reynolds number $k - \varepsilon$ turbulence model. A non-Boussinesq variable density approach is used to model the density variations. Simplified Marker and Cell (SMAC) algorithm is used to solve the governing equations on collocated grid with high accuracy compact finite difference schemes. The pressure Poisson equation is solved by bi-conjugate gradient algorithm and time integration is performed with four stage Runge–Kutta method (Rk-4). The results are presented for Grashof number $Gr = 10^{11}$ and 10^{12} and Gay-Lussac number $Ga = 0.2$ and 2 . The present model is valid when buoyancy effects are significant in comparison with forced convection effects. The heat transfer characteristics are analyzed by varying forced inlet velocity, inlet port size and inlet port location. The assisting flow enhances plume discharge rate and increases convective heat loss from cavity. The opposing flow weakens thermal buoyancy and minimizes convective heat loss from cavity. The present mathematical model and numerical method are in good agreement with the existing results available in the literature.

© 2015 Elsevier Inc. All rights reserved.

1. Introduction

The plume structures arising from the effects of thermal buoyancy and discharge rate through openings are of great importance in cooling of electronic devices, solar cavity receivers, building natural ventilation and enclosure fires. In buoyant flows, it is customary to adopt Boussinesq approximation to model thermal buoyancy force. However, for applications with high temperature difference such as nuclear reactor systems, heat generation stations, foundry processes and fire transport phenomena it is inappropriate to evaluate density variations by Boussinesq approximation. In naturally ventilated open cavities with internal heat source, heat and mass exchange through vertical and horizontal openings are generated because of density difference caused by temperature difference. The flow patterns through large vertical openings such as doorways and windows are well investigated in the literature. Brown and Solvason [1] studied the natural convection flow through single vertical rectangular openings in partitions. They determined neutral pressure level close to middle of opening height, and air flow profile through vertical openings develops stable velocity distribution. Prahla and Emmons [2] predicted the flow of fire gases through doorway of a burning room and proposed mathematical models to calculate exchange flow through vertical passages. Their model assumes

* Corresponding author. Tel.: +91 40 23016074; fax: +91 40 23016032.
E-mail address: kvenkat@iith.ac.in (K. Venkatasubbaiah).

Nomenclature

H	Height of the enclosure
W	Width of the enclosure
D	Horizontal vent width
H_v	Height of inlet port
T_s	Heat source temperature
T_∞	Initial fluid temperature
g	Gravitational force per unit mass
μ	Dynamic viscosity
μ_t	Turbulent dynamic viscosity
ρ	Fluid density
k	Turbulence kinetic energy
ϵ	Turbulent dissipation rate
U, V	Dimensionless velocity components along x and y directions
τ	Dimensionless time
θ	Dimensionless temperature
K	Dimensionless turbulence kinetic energy
ϵ	Dimensionless turbulent dissipation rate
Pr	Prandtl number
Pr_t	Turbulent Prandtl number
Gr	Grashof number
Ra	Rayleigh number
Ri	Richardson number
Ga	Gay-Lussac's number

the presence of two gas layers in the enclosure; upper layer filled with hot fire gases and lower air layer made up of entrained ambient air.

Mercier and Jaluria [3] conducted experiments on fire induced flow of hot gas in enclosure with vertical openings. They injected hot gases into the enclosure from lower opening and observed wall plume temperature pattern inside the enclosure. Similar experiments [4,5] were carried out to predict buoyancy induced ventilation rate in compartment with sidewall opening. Abib and Jaluria [6] did numerical simulation to evaluate the buoyant flow arising from fire source in vented compartment. They analyzed thermal plume behavior and calculated the bidirectional flow rates through opening by restricting the computational domain within the cavity. Chow and Zou [7] numerically studied airflow rates through doorway in fire scenarios and the proposed empirical correlations were in good agreement with experimental data. In the literature, similar CFD simulations [8–11] were reported to predict the air movement through vertical openings.

The flow patterns through horizontal openings are more complex and unstable than vertical openings. One of the earliest studies on natural convection flows through horizontal openings was carried out by Epstein [12]. He experimentally studied the bidirectional flows through horizontal circular opening with brine and fresh as fluid medium. Epstein varied the vent aspect ratio and proposed empirical model to calculate mass flow rate. Tan and Jaluria [13–15] did experiments to study the mass flow rate through a horizontal vent in an enclosure due to pressure and density differences. They identified the critical pressure at which transition from bidirectional to unidirectional flow occurs across the vent. Recently, Venkatasubbaiah and Jaluria [16] analyzed the fire driven flow in square enclosure with single and multiple ceiling vents. They varied vent size and found that the critical Grashof number is 10^6 , above this flow becomes chaotic inside the enclosure. Chow and Gao [17,18] investigated air flow patterns across horizontal vent and they identified that the ratio of buoyancy and inertia force is one of the key parameter affecting the bidirectional discharge across the opening. All the above studies concluded that flow patterns through horizontal vent is more complex and flow resistance is greater than in vertical opening. The transient behavior across the opening is due to the presence of denser fluid on top of lighter fluid and needs further understanding.

The buoyancy induced turbulent mixing is one of the key process for the growth and spread of thermal plume. Turbulent natural convection flow in differentially heated square cavity was studied by Markatos and Pericleous [19] using standard $k - \epsilon$ turbulence model. They identified that the model is suitable for predicting buoyant flows. Chattopadhyay and Saha [20] used large eddy simulation turbulence model to simulate the flow characteristics of impinging jet over a moving plate. They have reported that turbulent kinetic energy and heat transfer from the plate increases with rise in surface velocity. Cook and Lomas [21] analyzed buoyancy driven flows in enclosure using standard $k - \epsilon$ and RNG $k - \epsilon$ models. They found RNG $k - \epsilon$ model gave better results. Similarly, Stavrakakis and Markatos [22] analyzed the air flow patterns in one and two room enclosures containing a fire source. Abib and Jaluria [23] studied the turbulent penetrative and recirculating flow in partial enclosure with low Reynolds number model of Lam-Bremhorst. Similarly, Davidson [24], Gupta et al. [25], Harish and Venkatasubbaiah [26,27] carried out numerical analysis on buoyancy induced turbulent flows using Lam-Bremhorst model and found that this model has higher capability of predicting turbulent quantities reasonably well in regions near and away from the walls.

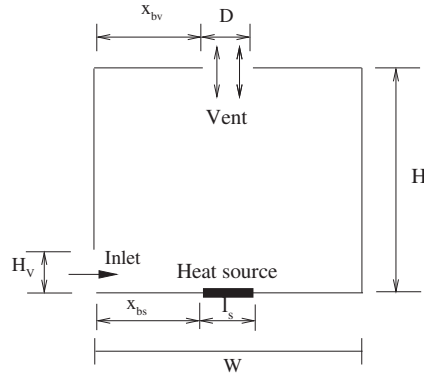


Fig. 1. Schematic diagram of ceiling vented square enclosure with inlet port.

In the literature, similar numerical studies on non-Boussinesq buoyancy induced flows were reported [28–31] in laminar flow regime. However, very few investigations [32,33] were presented by incorporating turbulence models. The turbulent flow characteristics through horizontal vent under the influence of forced inlet ports modeled by non-Boussinesq approach are limited in the literature. This has been the motivation for present investigation. In the present article, turbulent combined convection flow in ceiling vented square enclosure with forced inlet port is numerically investigated. A non-Boussinesq variable density approach is implemented to evaluate the density variations. Turbulence is modeled with two-equation Lam-Bremhorst low Reynolds number $k - \epsilon$ model. The results are presented by varying the Grashof number, forced inlet velocity and inlet port size. The assisting and opposing effects of forced inlet air stream are analyzed by changing the inlet port location.

2. Governing equations

Fig. 1 represents the schematic diagram of square enclosure with ceiling vent and inlet port. There is a finite size heat source of constant wall temperature T_s located at the bottom wall of enclosure. A horizontal vent of width D is opened to the ambient media and inlet port of height H_v facilitates the entry of forced air stream into the square enclosure. The turbulent combined convection flow is modeled as unsteady, two-dimensional, compressible flow problem suitable for low Mach number flows. The thermo-physical properties of fluid are constant, except the change in density that are evaluated from ideal gas law. The governing equations comprise the unsteady Favre averaged Navier–Stokes equation (UFANS) including the time average energy equation for mean temperature field. Turbulence is modeled with buoyancy modified Lam-Bremhorst low Reynolds number $k - \epsilon$ model. The dimensional forms of basic governing equations are as follows:

$$\frac{\partial \rho}{\partial t} + \frac{\partial(\rho u)}{\partial x} + \frac{\partial(\rho v)}{\partial y} = 0, \tag{1}$$

$$\begin{aligned} \frac{\partial(\rho u)}{\partial t} + \frac{\partial(\rho uu)}{\partial x} + \frac{\partial(\rho uv)}{\partial y} = & -\frac{\partial(p - p_\infty)}{\partial x} + \frac{\partial}{\partial x} \left(2\mu \frac{\partial u}{\partial x} - \frac{2}{3}\mu \left[\frac{\partial u}{\partial x} + \frac{\partial v}{\partial y} \right] \right) + \frac{\partial}{\partial y} \left(\mu \left[\frac{\partial u}{\partial y} + \frac{\partial v}{\partial x} \right] \right) \\ & + 2 \frac{\partial}{\partial x} \left[\mu_t \frac{\partial u}{\partial x} \right] + \frac{\partial}{\partial y} \left[\mu_t \frac{\partial u}{\partial y} \right] + \frac{\partial}{\partial y} \left[\mu_t \frac{\partial v}{\partial x} \right], \end{aligned} \tag{2}$$

$$\begin{aligned} \frac{\partial(\rho v)}{\partial t} + \frac{\partial(\rho uv)}{\partial x} + \frac{\partial(\rho vv)}{\partial y} = & -\frac{\partial(p - p_\infty)}{\partial y} + \frac{\partial}{\partial x} \left(\mu \left[\frac{\partial u}{\partial y} + \frac{\partial v}{\partial x} \right] \right) + \frac{\partial}{\partial y} \left(2\mu \frac{\partial v}{\partial y} - \frac{2}{3}\mu \left[\frac{\partial u}{\partial x} + \frac{\partial v}{\partial y} \right] \right) \\ & - (\rho - \rho_\infty)g + \frac{\partial}{\partial x} \left[\mu_t \frac{\partial u}{\partial y} \right] + \frac{\partial}{\partial x} \left[\mu_t \frac{\partial v}{\partial x} \right] + 2 \frac{\partial}{\partial y} \left[\mu_t \frac{\partial v}{\partial y} \right], \end{aligned} \tag{3}$$

$$\frac{\partial(\rho T)}{\partial t} + \frac{\partial(\rho uT)}{\partial x} + \frac{\partial(\rho vT)}{\partial y} = \frac{\partial}{\partial x} \left[\left(\frac{k}{C_p} + \frac{\mu_t}{Pr_t} \right) \frac{\partial T}{\partial x} \right] + \frac{\partial}{\partial y} \left[\left(\frac{k}{C_p} + \frac{\mu_t}{Pr_t} \right) \frac{\partial T}{\partial y} \right]. \tag{4}$$

The equation of state relates density with pressure and temperature and are as follows:

$$p = \rho RT, \tag{5}$$

$$\frac{\partial(\rho k)}{\partial t} + \frac{\partial(\rho u k)}{\partial x} + \frac{\partial(\rho v k)}{\partial y} = \frac{\partial}{\partial x} \left[\left(\mu + \frac{\mu_t}{\sigma_k} \right) \frac{\partial k}{\partial x} \right] + \frac{\partial}{\partial y} \left[\left(\mu + \frac{\mu_t}{\sigma_k} \right) \frac{\partial k}{\partial y} \right] - \frac{g\mu_t}{\sigma_t} \frac{\partial \rho}{\partial y} - \epsilon + \mu_t \left[2 \left(\frac{\partial u}{\partial x} \right)^2 + 2 \left(\frac{\partial v}{\partial y} \right)^2 + \left(\frac{\partial u}{\partial y} + \frac{\partial v}{\partial x} \right)^2 \right], \tag{6}$$

$$\frac{\partial(\rho \epsilon)}{\partial t} + \frac{\partial(\rho u \epsilon)}{\partial x} + \frac{\partial(\rho v \epsilon)}{\partial y} = \frac{\partial}{\partial x} \left[\left(\mu + \frac{\mu_t}{\sigma_\epsilon} \right) \frac{\partial \epsilon}{\partial x} \right] + \frac{\partial}{\partial y} \left[\left(\mu + \frac{\mu_t}{\sigma_\epsilon} \right) \frac{\partial \epsilon}{\partial y} \right] - C_{2\epsilon} f_2 \frac{\epsilon^2}{k} + C_{1\epsilon} f_1 \left[\mu_t \left\{ 2 \left(\frac{\partial u}{\partial x} \right)^2 + 2 \left(\frac{\partial v}{\partial y} \right)^2 + \left(\frac{\partial u}{\partial y} + \frac{\partial v}{\partial x} \right)^2 \right\} - C_{3\epsilon} \left\{ \frac{g\mu_t}{\sigma_t} \frac{\partial \rho}{\partial y} \right\} \right], \tag{7}$$

where g is the acceleration due to gravity; β is the coefficient of volumetric thermal expansion; ρ is the density of the fluid; ν is the kinematic viscosity; ν_t is the turbulent eddy viscosity; σ_t is the turbulent Prandtl number. The pressure work and viscous dissipation terms in energy equation are ignored for low Mach number flows. Further details on pressure Poisson equation are reported in [34].

The following non-dimensional variables are used to obtain the dimensionless governing equations:

The free convection velocity ($V_c = \sqrt{g\beta\Delta TH}$) is considered as the reference velocity scale. $X = \frac{x}{H}$; $Y = \frac{y}{H}$; $U = \frac{u}{V_c}$; $V = \frac{v}{V_c}$; $\tau = \frac{tV_c}{H}$; $\theta = \frac{T-T_\infty}{T_s-T_\infty}$; $V_c = (g\beta\Delta TH)^{\frac{1}{2}}$; $P = \frac{p-p_\infty}{\rho_\infty V_c^2}$; $Q = \frac{\rho}{\rho_\infty}$; $K = \frac{k}{(g\beta\Delta TH)}$; $E = \frac{\epsilon}{(g\beta\Delta T)^{\frac{3}{2}} H^{\frac{1}{2}}}$.

The non-dimensional form of governing equations is as follows:

$$\frac{\partial Q}{\partial \tau} + \frac{\partial(QU)}{\partial X} + \frac{\partial(QV)}{\partial Y} = 0, \tag{8}$$

$$\frac{\partial(QU)}{\partial \tau} + \frac{\partial(QUU)}{\partial X} + \frac{\partial(QUV)}{\partial Y} = -\frac{\partial P}{\partial X} + \frac{\partial}{\partial X} \left(\frac{2}{(Gr)^{\frac{1}{2}}} \frac{\partial U}{\partial X} - \frac{2}{3(Gr)^{\frac{1}{2}}} \left[\frac{\partial U}{\partial X} + \frac{\partial V}{\partial Y} \right] \right) + \frac{\partial}{\partial Y} \left(\frac{1}{(Gr)^{\frac{1}{2}}} \left[\frac{\partial U}{\partial Y} + \frac{\partial V}{\partial X} \right] \right) + 2 \frac{\partial}{\partial X} \left[\frac{1}{Re_t} \frac{\partial U}{\partial X} \right] + \frac{\partial}{\partial Y} \left[\frac{1}{Re_t} \frac{\partial U}{\partial Y} \right] + \frac{\partial}{\partial Y} \left[\frac{1}{Re_t} \frac{\partial V}{\partial X} \right], \tag{9}$$

$$\frac{\partial(QV)}{\partial \tau} + \frac{\partial(QUV)}{\partial X} + \frac{\partial(\rho VV)}{\partial Y} = -\frac{\partial P}{\partial Y} + \frac{\partial}{\partial X} \left(\frac{1}{(Gr)^{\frac{1}{2}}} \left[\frac{\partial U}{\partial Y} + \frac{\partial V}{\partial X} \right] \right) - \frac{(\rho - 1)}{Ga} + \frac{\partial}{\partial Y} \left(\frac{2}{(Gr)^{\frac{1}{2}}} \frac{\partial V}{\partial Y} - \frac{2}{3(Gr)^{\frac{1}{2}}} \left[\frac{\partial U}{\partial X} + \frac{\partial V}{\partial Y} \right] \right) + \frac{\partial}{\partial X} \left[\frac{1}{Re_t} \frac{\partial U}{\partial Y} \right] + \frac{\partial}{\partial X} \left[\frac{1}{Re_t} \frac{\partial V}{\partial X} \right] + 2 \frac{\partial}{\partial Y} \left[\frac{1}{Re_t} \frac{\partial V}{\partial Y} \right], \tag{10}$$

$$\frac{\partial(Q\theta)}{\partial \tau} + \frac{\partial(QU\theta)}{\partial X} + \frac{\partial(\rho V\theta)}{\partial Y} = \frac{\partial}{\partial X} \left[\left(\frac{1}{(Pr(Gr)^{\frac{1}{2}})} + \frac{1}{Pr_t Re_t} \right) \frac{\partial \theta}{\partial X} \right] + \frac{\partial}{\partial Y} \left[\left(\frac{1}{(Pr(Gr)^{\frac{1}{2}})} + \frac{1}{Pr_t Re_t} \right) \frac{\partial \theta}{\partial Y} \right], \tag{11}$$

$$\frac{\partial(QK)}{\partial \tau} + \frac{\partial(QUK)}{\partial X} + \frac{\partial(\rho VK)}{\partial Y} = \frac{\partial}{\partial X} \left[\left(\frac{1}{(Gr)^{\frac{1}{2}}} + \frac{1}{\sigma_k Re_t} \right) \frac{\partial K}{\partial X} \right] + \frac{\partial}{\partial Y} \left[\left(\frac{1}{(Gr)^{\frac{1}{2}}} + \frac{1}{\sigma_k Re_t} \right) \frac{\partial K}{\partial Y} \right] - \frac{1}{Re_t \sigma_t} \frac{\partial Q}{\partial Y} - \epsilon + \frac{1}{Re_t} \left[2 \left(\frac{\partial U}{\partial X} \right)^2 + 2 \left(\frac{\partial V}{\partial Y} \right)^2 + \left(\frac{\partial U}{\partial Y} + \frac{\partial V}{\partial X} \right)^2 \right], \tag{12}$$

$$\frac{\partial(Q\epsilon)}{\partial \tau} + \frac{\partial(QU\epsilon)}{\partial X} + \frac{\partial(\rho V\epsilon)}{\partial Y} = \frac{\partial}{\partial X} \left[\left(\frac{1}{(Gr)^{\frac{1}{2}}} + \frac{1}{\sigma_\epsilon Re_t} \right) \frac{\partial \epsilon}{\partial X} \right] + \frac{\partial}{\partial Y} \left[\left(\frac{1}{(Gr)^{\frac{1}{2}}} + \frac{1}{\sigma_\epsilon Re_t} \right) \frac{\partial \epsilon}{\partial Y} \right] - C_{2\epsilon} f_2 \frac{\epsilon^2}{k} - C_{1\epsilon} f_1 \left[\frac{1}{Re_t} \left\{ 2 \left(\frac{\partial U}{\partial X} \right)^2 + 2 \left(\frac{\partial V}{\partial Y} \right)^2 + \left(\frac{\partial U}{\partial Y} + \frac{\partial V}{\partial X} \right)^2 \right\} - C_{3\epsilon} \frac{1}{Re_t \sigma_t} \frac{\partial Q}{\partial Y} \right] \frac{\epsilon}{K}. \tag{13}$$

For low Reynolds number $k - \epsilon$ turbulence model, constants used are $C_\mu = 0.09$; $C_{1\epsilon} = 1.44$; $C_{2\epsilon} = 1.92$; $C_{3\epsilon} = 0.7$; $Pr_t = 0.9$; $\sigma_k = 1.0$; $\sigma_\epsilon = 1.3$. The damping wall functions f_1 , f_2 and f_μ are as follows:

$$f_1 = 1 + \left(\frac{0.14}{f_\mu} \right)^3, \tag{14}$$

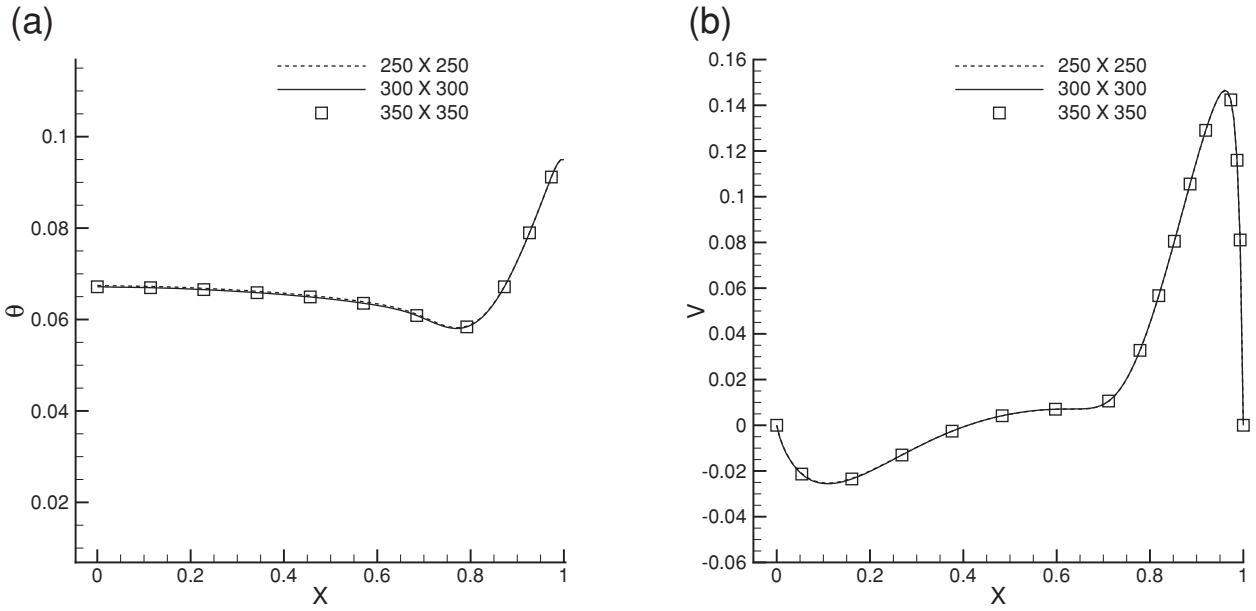


Fig. 2. Midheight temperature distribution and normal velocity profiles for $Gr = 10^{12}$; $\alpha = 0.1$.

Table 1
Average Nusselt number variation for different grids.

Grid size	Average Nusselt number
250 × 250	115.147
300 × 300	115.279
350 × 350	115.275

$$f_2 = [1 - 0.27 \exp(-R_t^2)][1 - \exp(-R_n)], \tag{15}$$

$$f_\mu = \exp\left[-\frac{3.4}{1 + \left(\frac{R_t}{50}\right)^2}\right], \tag{16}$$

where $Gr = \frac{g\beta\Delta TH^3}{\nu^2}$ is the Grashof number; $Ga = \beta\Delta T$ indicates Gay-Lussac's number; $Pr = \frac{\nu}{\alpha_t}$ represents Prandtl number; α_t is the thermal diffusivity; $Re_t = \frac{E}{C_\mu \rho K^2}$; $R_t = Gr^{1/2} \left(\frac{K^2}{E}\right)$; $R_n = Gr^{1/2} K^{1/2} n$; n is the normal distance from the nearest wall.

3. Boundary conditions

At the vent opening, mass and energy exchange occurs and flow modeling is complex due to the bidirectional exchange of hot and cold fluids. Chan and Tien [35] predicted accurate results by restricting the computational domain within the cavity. The solid walls are treated with adiabatic boundary conditions and no-slip boundary conditions are specified for velocity fields. The temperature of the heat source is specified with constant wall temperature. Across the horizontal vent, longitudinal velocity is set to zero and normal velocity is obtained from mass balance $\frac{\partial V}{\partial Y} = 0$. The temperature of fluid leaving through the vent satisfies the upwind boundary condition $\frac{\partial \theta}{\partial Y} = 0$. In solid walls, turbulent kinetic energy and normal gradient of dissipation is set to zero. At the vent, the normal gradients of kinetic energy and dissipation are set to zero. Uniform velocity and temperature field are specified across the inlet port. The dimensionless longitudinal velocity of ambient air at the inlet port is defined as follows:

$$\alpha = \frac{u_\infty}{V_c} = \frac{u_\infty}{\sqrt{g\beta\Delta TH}} = \frac{Re}{Gr^{0.5}} = \frac{1}{\sqrt{Ri}}, \tag{17}$$

where $Ri = \frac{Gr}{Re^2}$ is the Richardson number. The Richardson number provides the measure of free convection in comparison with the forced convection.

Table 2
Validation of average Nusselt number.

Rayleigh number	Present	Dixit and Babu [37]
10^8	30.142	30.506
10^9	56.927	57.350
10^{10}	104.758	103.663

The appropriate initial and boundary conditions in dimensionless form are as follows:

$$\text{at } \tau = 0 : U = V = \theta = 0, \tag{18}$$

$$\text{for } \tau > 0 : X = 0; X = 1.0; 0 < Y < 1.0 : U = V = \frac{\partial \theta}{\partial X} = \frac{\partial P}{\partial X} = K = \frac{\partial \varepsilon}{\partial X} = 0;$$

$$X = 0; 0 < Y < H_v : V = \theta = P = 0; U = \frac{1}{\sqrt{Ri}}, \tag{19}$$

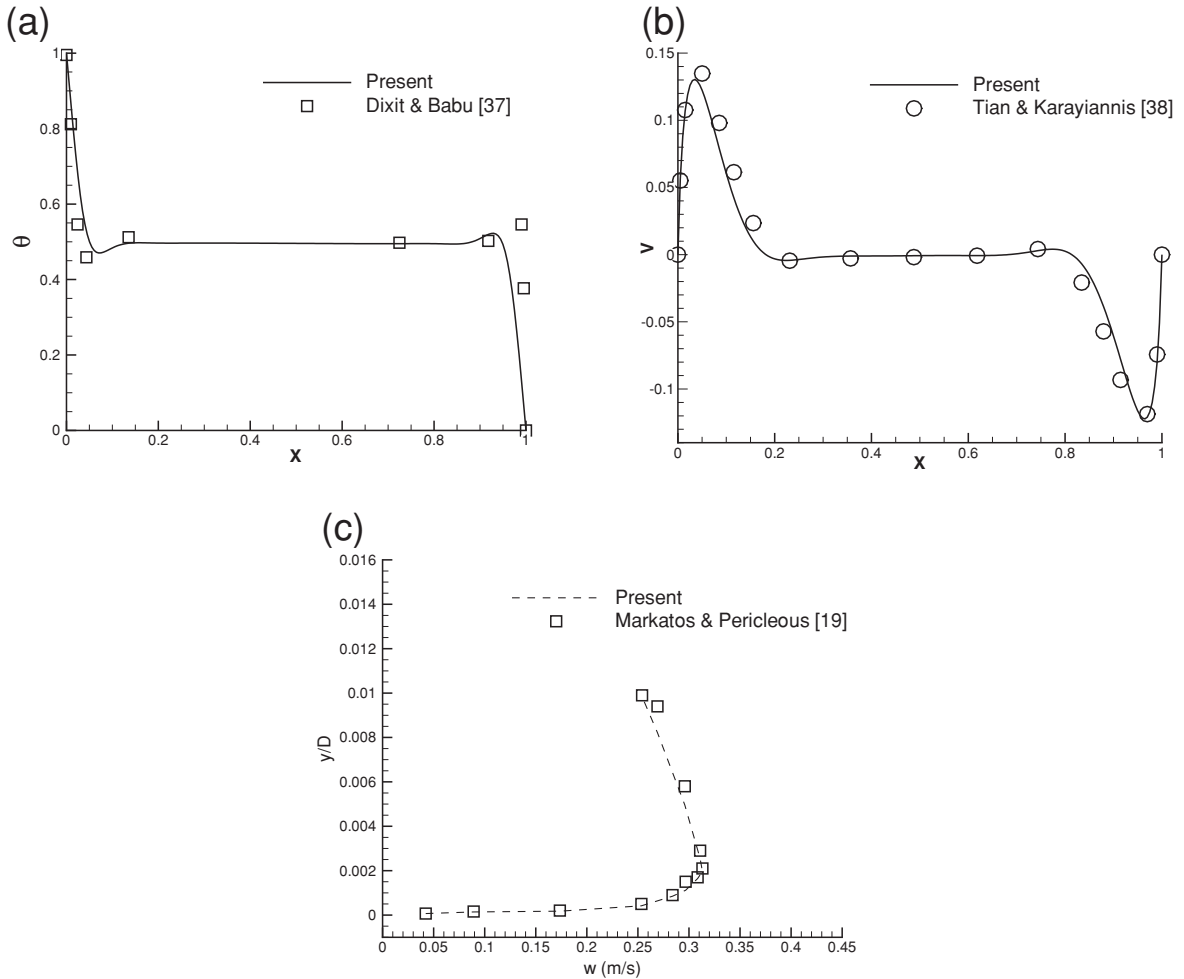


Fig. 3. Validation of present results with benchmark results (a) temperature profile, (b) normal velocity profile and (c) normal velocity profile plotted at $z/D = 0.5$.

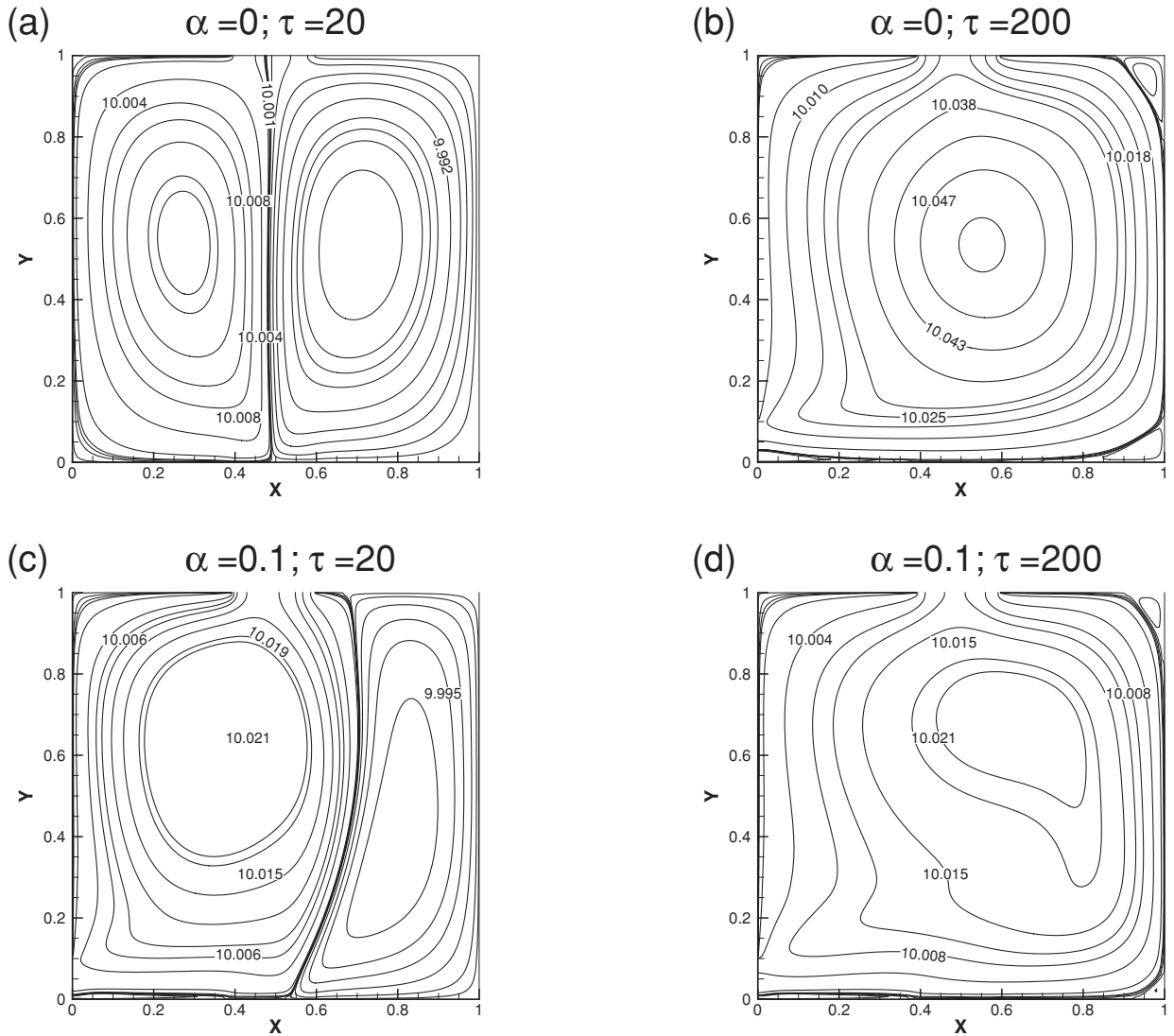


Fig. 4. Evolution of stream function contours for different inlet velocities.

$$Y = 0; 0 < X < 1.0 : U = V = \frac{\partial \theta}{\partial Y} = \frac{\partial P}{\partial Y} = K = \frac{\partial \varepsilon}{\partial Y} = 0$$

$$Y = 0; 0 < X < X_{bs} : \frac{\partial \theta}{\partial Y} = 0$$

$$X_{bs} < X < X_{bs} + l_s : \theta = 1.0$$

$$X_{bs} + l_s < X < 1.0 : \frac{\partial \theta}{\partial Y} = 0$$

(20)

$$Y = 1.0; 0 < X < X_{bv} : U = V = \frac{\partial \theta}{\partial Y} = \frac{\partial P}{\partial Y} = K = \frac{\partial \varepsilon}{\partial Y} = 0$$

$$X_{bv} < X < X_{bv} + D : U = P = \frac{\partial V}{\partial Y} = \frac{\partial \theta}{\partial Y} = \frac{\partial K}{\partial Y} = \frac{\partial E}{\partial Y} = 0,$$

$$X_{bv} + D < X < 1.0 : U = V = \frac{\partial \theta}{\partial Y} = \frac{\partial P}{\partial Y} = K = \frac{\partial \varepsilon}{\partial Y} = 0,$$

(21)

where X_{bs} is the distance up to the source; l_s is the source width; X_{bv} is the distance up to the vent; D is the vent width.

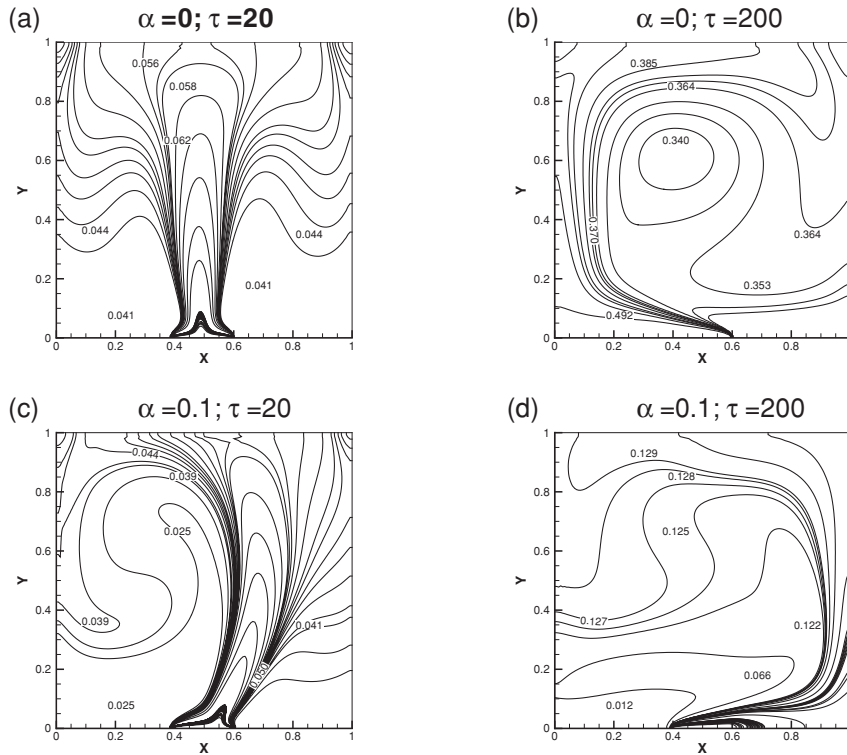


Fig. 5. Evolution of temperature contours for different inlet velocities.

4. Numerical procedure

The governing equations are solved by finite difference method and the solver is developed in Fortran 90. Simplified Marker and Cell (SMAC) algorithm is used to solve the governing equations on collocated grid. The pressure velocity decoupling is avoided by using Rhie–Chow momentum interpolation technique. The second order central finite difference schemes are used to discretize diffusion terms; meanwhile, non-linear convective terms are evaluated using high accuracy compact schemes [36]. The pressure Poisson equation is solved by bi-conjugate gradient algorithm. The convergence criterion is set as 10^{-6} to solve the pressure Poisson equation. The residual is normalized with pressure value of previous iteration. The remaining governing equations are marched with a small time step of 10^{-4} . Time integration is performed by four stages Runge–Kutta (RK-4) method. The CPU time required for a typical run was around 30 h. The simulations were performed in an Intel Xenon workstation with a configuration of 2.27 GHz and 12 GB RAM.

5. Grid independence and validation

The grid independence test is performed with three different mesh sizes. Fig. 2 indicates the variation of temperature and normal velocity profiles along the horizontal wall at the mid-height of square enclosure for $Gr = 10^{12}$ and $\alpha = 0.1$. From the temperature and velocity profiles, it is observed that solution is grid independent with mesh size of 300×300 . Moreover, Table 1 indicates the averaged Nusselt number along the heated wall estimated for three grid sizes. The local Nusselt number along the heated wall is numerically integrated by trapezoidal rule to obtain the average Nusselt number. The deviations in the average Nusselt number values predicted with three different grid sizes are insignificant and hence all simulations are reported with grid size of 300×300 .

The accuracy of the present numerical model and the method of solution are compared with numerical and experimental results available in the literature. Table 2 summarizes the quantitative comparison of average Nusselt number with differentially heated square cavity results of Dixit and Babu. It is noticed that the present results are closer to the benchmark results of Dixit and Babu [37]. Further validations are performed with experimental benchmark results of Tian and Karayiannis [38] for $Ra = 1.58 \times 10^9$. The average Nusselt number reported by Tian and Karayiannis was 64. The average Nusselt number obtained using the present numerical model is 63.6. The present numerical method with compact schemes is closer to the benchmark results reported in the literature. Fig. 3(a) indicates the comparison of temperature profiles along the horizontal wall at the center of the differentially heated cavity for $Ra = 10^8$. Fig. 3(b) represents the comparison of normal velocity profiles with the experimental

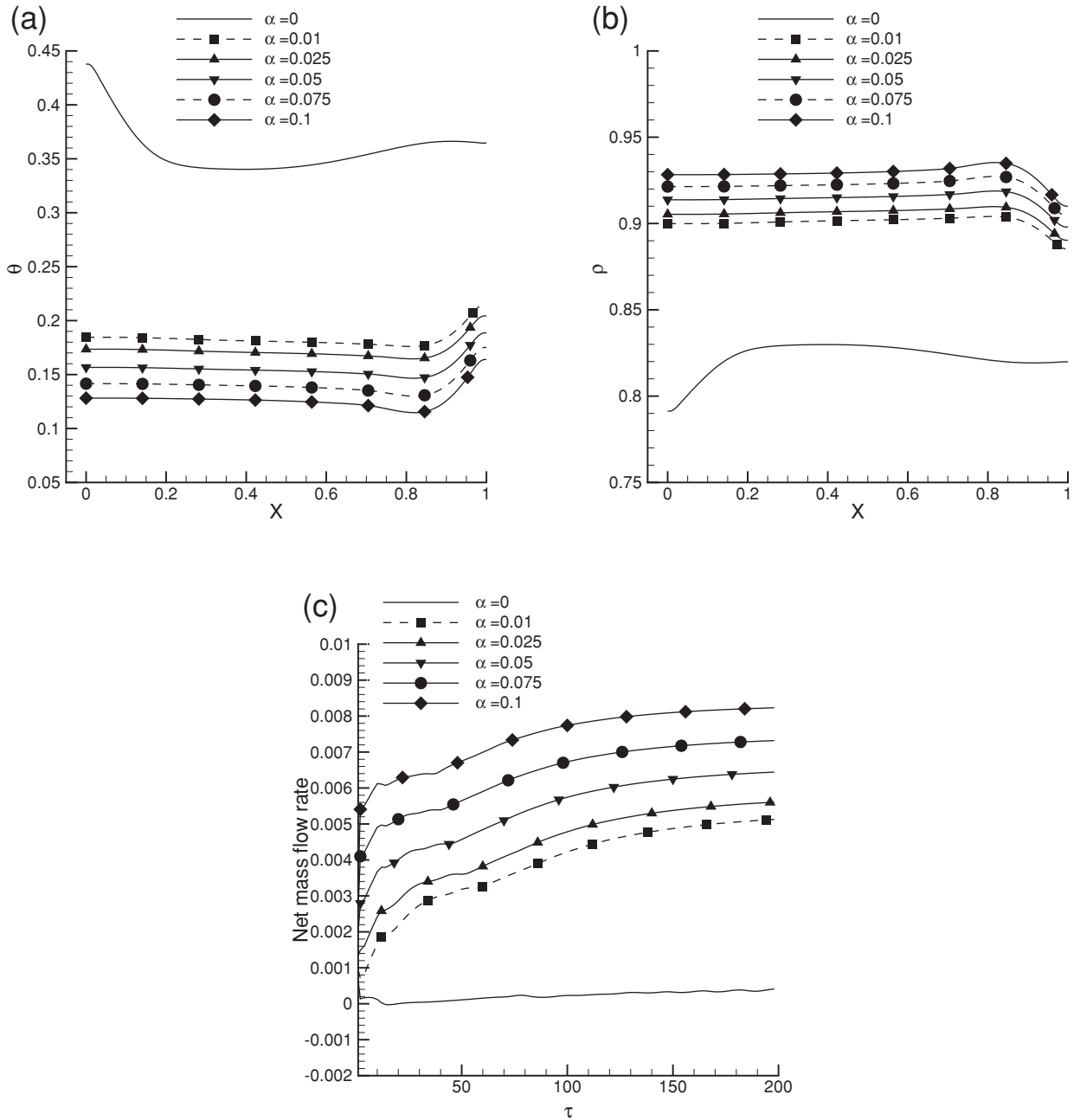


Fig. 6. Comparison of midheight (a) temperature profile, (b) density profile and (c) net mass flow rates for different inlet velocities.

results of Tian and Karayiannis [38] for $Ra = 1.58 \times 10^9$. Further validations are performed in Fig. 3(c) by comparing the normal velocity profiles within boundary layer with the benchmark results of Markatos and Pericleous [19] for $Ra = 10^{12}$, $z/D = 0.5$. From Fig. 3, it is noticed that the present results are in good agreement with the benchmark results reported in the literature [19,37,38].

6. Results and discussions

Numerical investigations are performed to study the thermal plume behavior in ceiling vented square enclosure. The schematic diagram is shown in Fig. 1. An inlet port is located along the left boundary to facilitate the entry of ambient air into the enclosure. The Prandtl number of air is fixed as 0.72. The value of Gay-Lussac number (Ga) for $Gr = 10^{11}$ and 10^{12} are

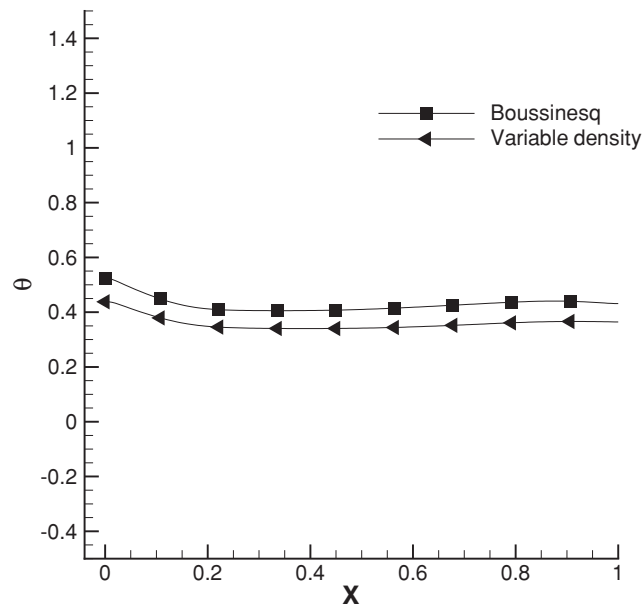


Fig. 7. Comparison of midheight temperature profiles with Boussinesq and non-Boussinesq approach.

0.2 and 2. The temperature difference used in the computation of $Gr = 10^{11}$ and $Ga = 0.2$ is 58.3°C and $Gr = 10^{12}$ and $Ga = 2$ is 583°C . Results are presented for different inlet velocity and Grashof number. Further investigations are performed by varying inlet port size and location.

6.1. Effect of inlet velocity

Figs. 4 and 5 characterizes the evolution of stream function and temperature contours with and without forced inlet velocity. The width of the ceiling vent is $0.2H$ and the Grashof number is 10^{11} . An inlet port of size $H_v = 0.1H$ is located at the bottom portion of left boundary at $0.05H$. The stream function contours indicate the evolution of convective cell patterns that arises due to the density difference between the hot and cold fluids. For $\alpha = 0$, at time interval $\tau = 20$, primary and secondary convective cells of equal strengths are formed inside the cavity. As flow progresses, two convective cells merges to form unicellular pattern inside the enclosure. In Fig. 4(c) and (d), forced ambient air penetrates through the inlet port and strength of primary convective cell is greater than the secondary cell. The inlet air stream assists the buoyancy force and increases the outflow of hot fluid through bidirectional ceiling vent.

In Fig. 5(a), axisymmetric plume evolves from the heat source, reaches the ceiling vent and spreads downward. The plume is vented through horizontal passage and density difference drives ambient fluid to creep into the enclosure. The entrained air fills the right half of the enclosure and tilts thermal plume toward left boundary. Hence, in Fig. 5(b) plume inclines and loses its momentum by impinging on left wall. For $\alpha = 0.1$, the longitudinal air stream tilts thermal plume toward right boundary. A wall plume structure develops across the right boundary.

Fig. 6 (a) and (b) indicates the variation of temperature and density profiles along the horizontal wall at the center of square cavity. It is evident that by increasing inlet port velocity $\alpha = 0.01$ – 0.1 , the mid-height temperature distribution drastically decreases. The rise in inlet velocity assists the plume outflow rate through ceiling opening, and increases the convection heat loss from the cavity. Moreover, significant amount of cold fluid enters through inlet port and ceiling vent and reduces plume temperature. Hence, the mid-height density profiles increases with rise in inlet velocity.

Fig. 6 (c) represents the variation of net mass flow rate through ceiling vent with different inlet velocity. The mass flow rate is calculated from the relation $m = \rho AV$, where A indicates the ceiling vent cross sectional area, ρ and V represents fluid density and normal velocity which are numerically integrated by trapezoidal rule. For $\alpha = 0$, the bidirectional exchange of hot and cold fluids are equal. Hence, the net mass flow rate magnitudes are close to zero. The net mass flow rate increases with rise in inlet velocity. The positive magnitudes indicate that plume discharge rate is higher in comparison to ambient entrainment rate.

Fig. 7 indicates the comparison of mid-height temperature profile predicted by present non-Boussinesq and Boussinesq models for $Gr = 10^{11}$ and $\alpha = 0.1$. The temperature values estimated by Boussinesq models are higher in comparison with non-Boussinesq models. The deviations visualized in the temperature profiles are due to the difference in modeling of buoyancy force. The average Nusselt number estimated for Boussinesq and non-Boussinesq models are 107.53 and 105.86 respectively. It is identified that Boussinesq model over-predicts the temperature and Nusselt number variation.

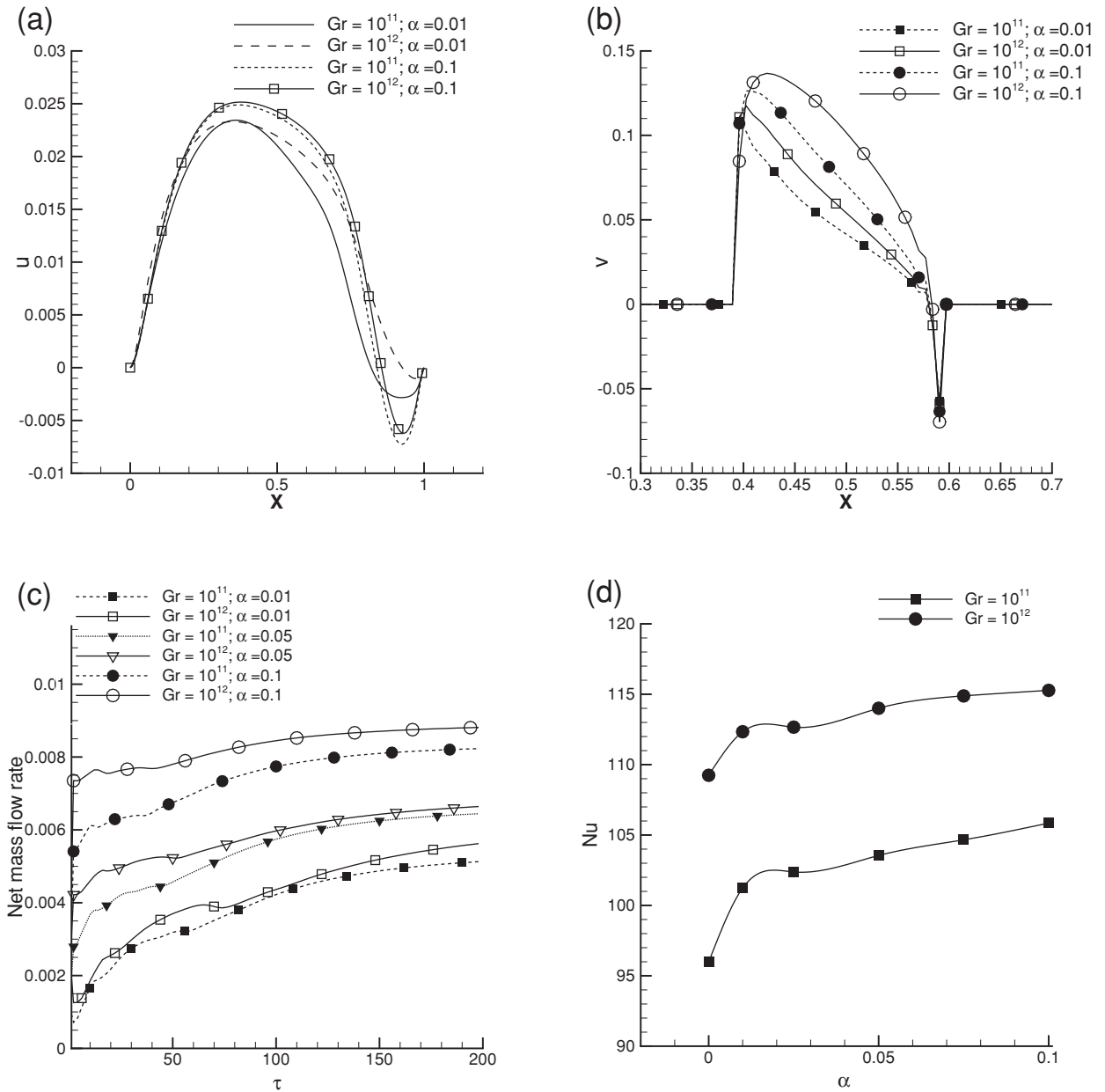


Fig. 8. Effect of Gr and alpha on (a) midheight longitudinal velocity profile; (b) normal velocity profiles across horizontal vent; (c) net mass flow rates and (d) average Nusselt number.

6.2. Effect of Grashof number

Fig. 8 (a) indicates the variation of mid-height longitudinal velocity for two different Grashof numbers 10¹¹ and 10¹² and inlet velocity alpha = 0.01 and 0.1. With rise in Grashof number and inlet velocity, the base temperature difference and plume velocity increases and the location of peak longitudinal velocity is along the midsection of the square cavity. The normal velocity profiles across the horizontal opening are plotted in Fig. 8(b) for Gr = 10¹¹ and 10¹² and alpha = 0.01 and 0.1. The positive and negative sign across the vent indicates hot and cold fluid velocities. It can be seen that the ambient entrainment rate is relatively very small in comparison with plume venting rate. Fig. 8(c) represents the variation of ceiling vent net mass flow rates for different inlet velocity. The heat loss from the cavity increases by varying inlet velocity alpha from 0.01 to 0.1. The forced air stream assists buoyancy force and accelerates the plume out flow rate. Hence by increasing alpha, a steep rise in the net mass flow rate values is visible across the horizontal opening.

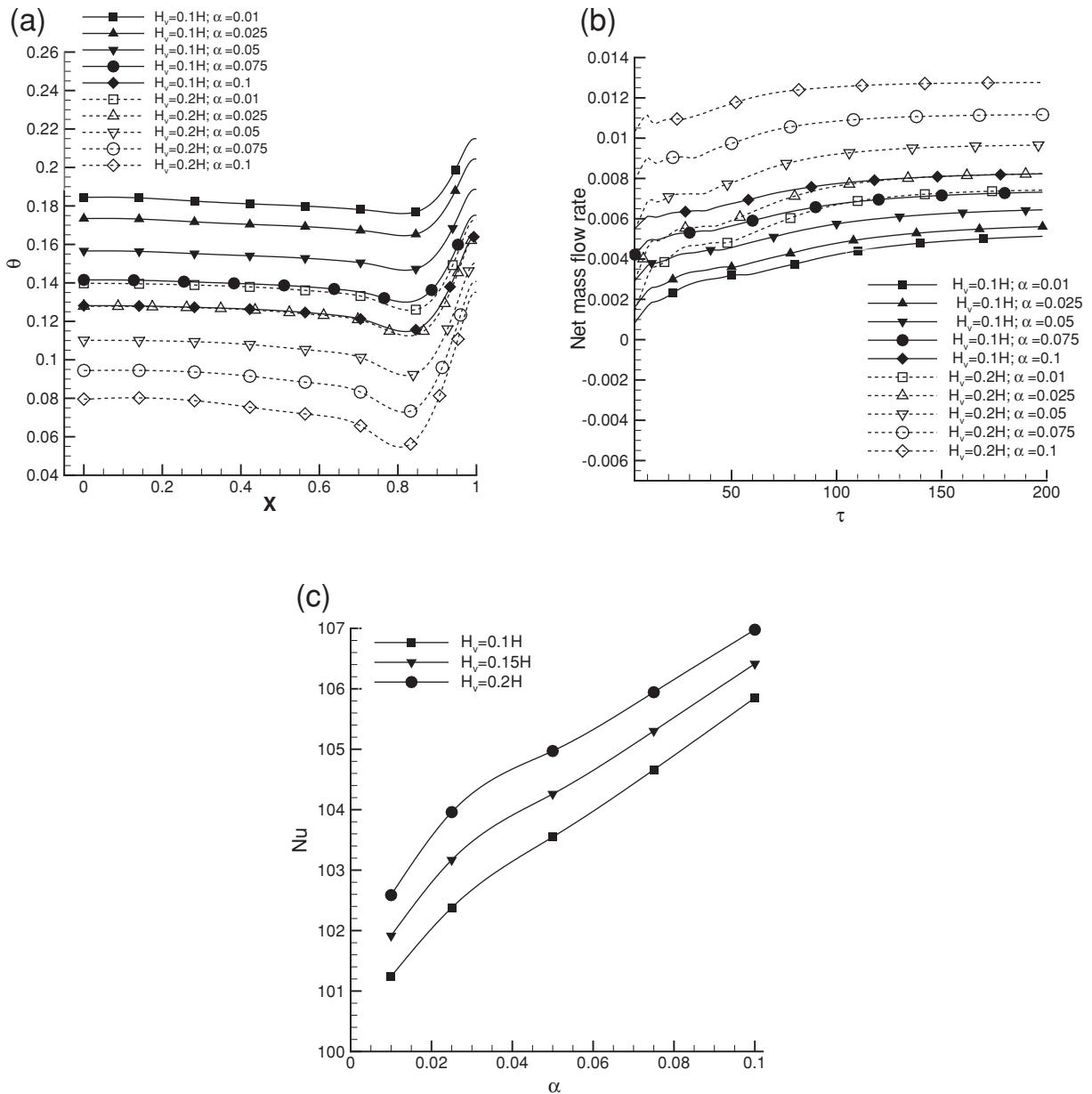


Fig. 9. Comparison of midheight (a) temperature profile, (b) net mass flow rates and (c) average Nusselt number for different H_v and α .

Fig. 8 (d) shows the plots of average Nusselt number by varying Gr and α . For $Gr = 10^{11}$, α is varied from 0.0 to 0.1 and the average Nusselt number increases by 5.4%, 6.6%, 7.8%, 9% and 10.2% respectively. From the Nusselt number plots it is evident that heat loss from the cavity increases with rise in inlet velocity. Moreover, a rise in Grashof number enhances heat transfer rate and the average Nusselt number for $Gr = 10^{12}$ is 11% higher in comparison with $Gr = 10^{11}$.

6.3. Effects of inlet port opening height (H_v)

The investigations are performed for inlet port opening height H_v varied from 0.1H to 0.2H for $Gr = 10^{11}$. Fig. 9(a) represents the variation of temperature profiles along the horizontal wall plotted at the mid-height of square cavity for $H_v = 0.1H$ and 0.2H and $\alpha = 0.01$ –0.1. It is visualized that with increase in inlet port height, significant amount of ambient fluid enters the cavity, and reduces the plume temperature. For $H_v = 0.2H$, and α varied from 0.01 to 0.1, the plume temperature decreases by 24.3%, 26.7%, 28.6%, 30.5% and 33.2% respectively. A comparison of net mass flow rate through the ceiling vent is shown in Fig. 9(b) for

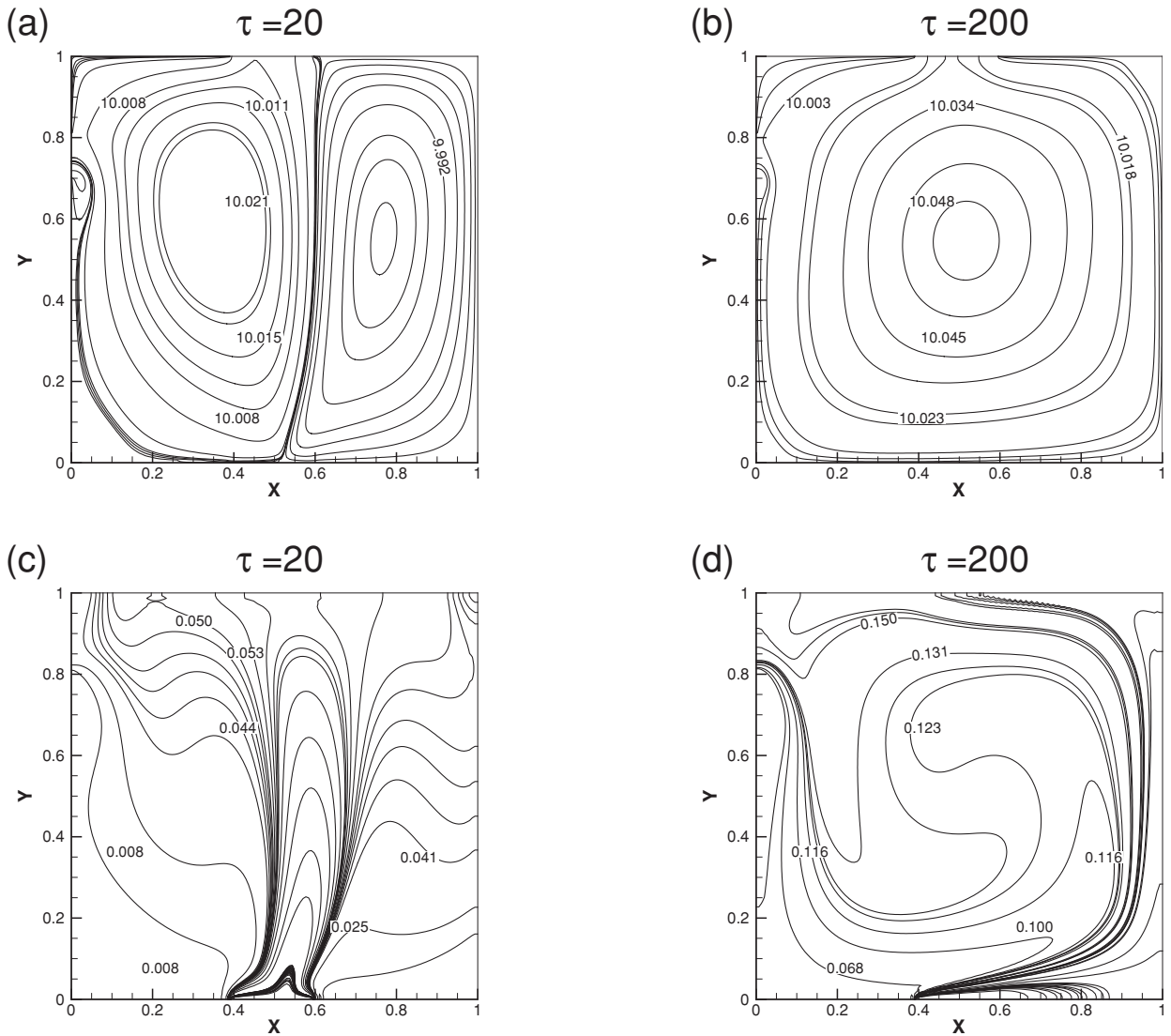


Fig. 10. Evolution of stream function (a, b) and temperature (c, d) contours for $V_L = 0.75H$; $\alpha = 0.1$.

different H_v and α . The assisting flow through inlet port strengthens the plume spread and further increases the discharge of hot fluid through ceiling vent. Hence the net mass flow rate increases with H_v and α .

The average Nusselt number variation for different H_v and α are plotted in Fig. 9(c). The forced ambient inlet intensifies the heat transfer rate and the average Nusselt number increases with H_v and α .

6.4. Effects of inlet port location (V_L)

The illustrations shown in Fig. 10 indicate the stream function (a and b) and temperature (c and d) contours for $Gr = 10^{11}$. The width of the centrally located ceiling vent is $0.2H$. A forced inlet port of height $H_v = 0.1H$ is located at $\frac{3}{4}H$ of the left boundary. The forced air stream increases the strength of primary convective cell and well mixed unicellular pattern is visualized at $\tau = 200$. The opposing flow distorts the symmetric pattern of thermal plume, weakens thermal buoyancy force and shifts the plume movement toward right boundary. The temperature distribution along the horizontal wall at the center of square enclosure is plotted in Fig. 11(a) for different V_L and α . The opposing flow reduces the convective heat loss from the cavity and increases the temperature concentration inside the enclosure. The mid-height temperature values increases with V_L and α .

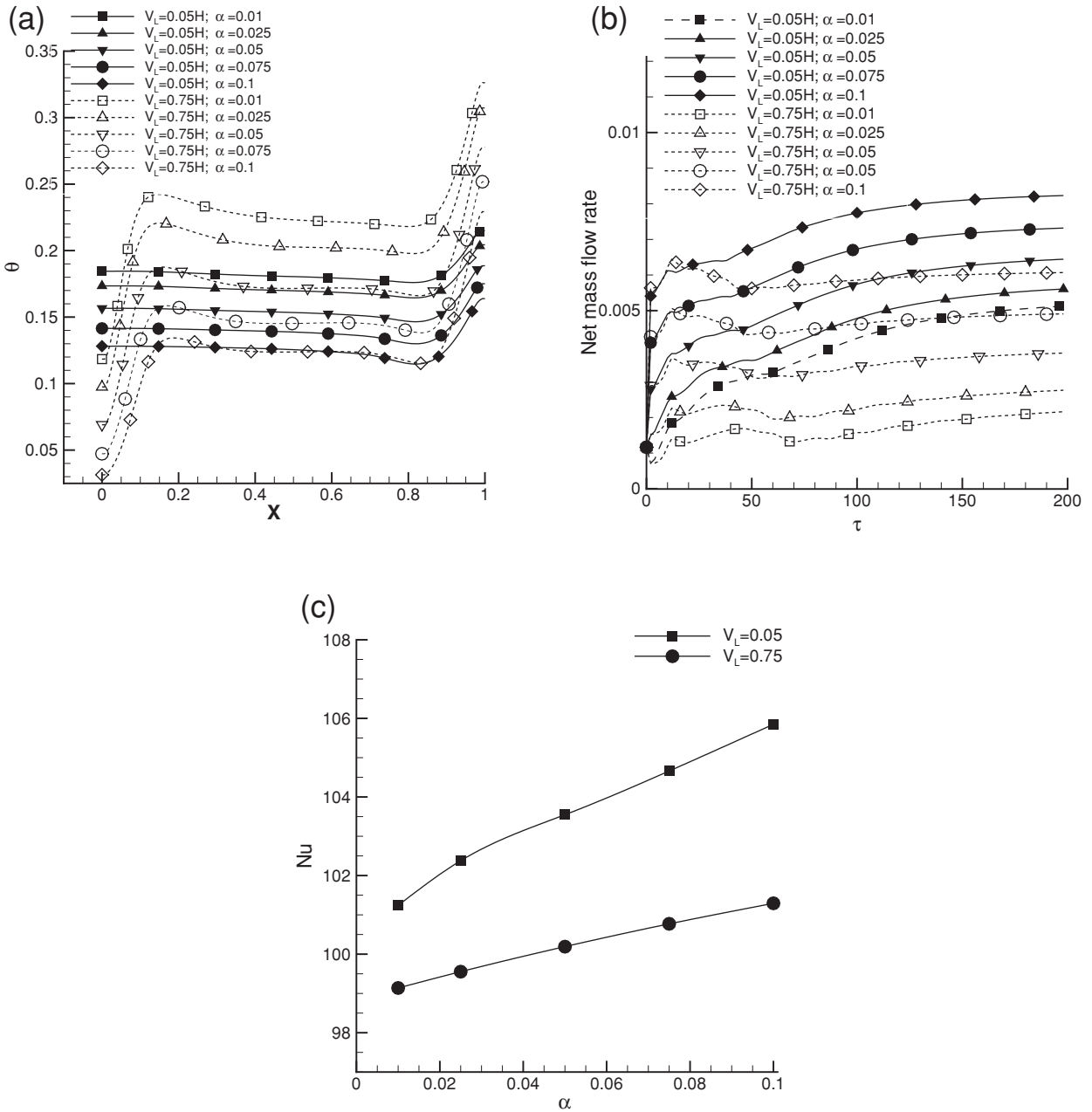


Fig. 11. Comparison of midheight (a) temperature distribution (b) net mass flow rate (c) average Nusselt number for different inlet port location and α .

The effect of inlet port location V_L on net mass flow rate through ceiling vent is represented in Fig. 11(b). The forced air stream suppresses the buoyancy force and reduces the bidirectional exchange rate through vent. Hence, the net mass flow rates are significantly less for $V_L = 0.75H$ in comparison to $V_L = 0.05H$. Fig. 11(c) illustrates the comparison of average Nusselt number by varying V_L and α . The convective heat loss from the cavity is minimized and the average Nusselt number values drops linearly with V_L and α . There is a 2–4.5% decrease in the average Nusselt number for $V_L = 0.75H$ in comparison to $V_L = 0.05H$.

7. Conclusions

The buoyancy dominated combined convection flow in partially open enclosure with forced inlet port is numerically studied. The bidirectional exchange rates through ceiling vent are investigated by varying Grashof number, forced longitudinal velocity and inlet port location. For assisting flow case, forced air stream strengthens thermal buoyancy force and increases plume

discharge rate through ceiling vent. This increased the convective heat loss from cavity, and temperature magnitudes decreased significantly inside the cavity. The average Nusselt number increases with longitudinal velocity. The vent discharge rate increases with rise in Grashof number and the average Nusselt number for $Gr = 10^{12}$ is increased by 11%. An increase in inlet port height intensifies net mass flow rate through ceiling vent and decreases the temperature distribution inside the enclosure. The opposing flow weakens thermal buoyancy force and minimizes the convective heat loss from cavity. The opposing forced air stream reduces bidirectional exchange through ceiling vent. The present results are useful for understanding the growth and spread of thermal plume inside a vented enclosure.

References

- [1] W.G. Brown, K.R. Solvason, Natural convection through rectangular openings in partitions-1: vertical partitions, *Int. J. Heat Mass Transf.* 163 (1962) 859–868.
- [2] J. Prahl, H.W. Emmons, Fire induced flow through an opening, *Combust. Flame* 25 (1975) 369–385.
- [3] G.P. Mercier, Y. Jaluria, Fire-induced flow of smoke and hot gases in open vertical enclosures, *Exp. Therm. Fluid Sci.* 19 (1999) 77–84.
- [4] S.E. Ozcan, E. Vranken, E. Berckmans, Measuring ventilation rate through naturally ventilated air openings by introducing heat flux, *Build. Environ.* 44 (2009) 27–33.
- [5] J. Tanny, V. Haslavsky, M. Teitel, Airflow and heat flux through the vertical opening of buoyancy-induced naturally ventilated enclosures, *Energy Build.* 40 (2008) 637–646.
- [6] A.H. Abib, Y. Jaluria, Numerical simulation of the buoyancy induced flow in a partially open enclosure, *Numer. Heat Transf. Part A* 14 (1988) 235–254.
- [7] W.K. Chow, G.W. Zou, Correlation equations on fire-induced air flow rates through doorway derived by large eddy simulation, *Build. Environ.* 40 (2005) 897–906.
- [8] P. Favarolo, H. Manz, Temperature-driven single-sided ventilation through a large rectangular opening, *Build. Environ.* 40 (2005) 689–699.
- [9] P. Ravikumar, D. Prakash, Analysis of thermal comfort in an office room by varying the dimensions of the windows on adjacent walls using CFD: a case study based on numerical simulation, *Build. Simul.* 2 (2009) 187–196.
- [10] J.O. Cheung, C.H. Liu, Cfd simulations of natural ventilation behaviour in high-rise buildings in regular and staggered arrangements at various spacings, *Energy Build.* 43 (2011) 1149–1158.
- [11] C. Allocca, Q. Chen, L.R. Glicksman, Design analysis of single-sided natural ventilation, *Energy Build.* 35 (2003) 785–795.
- [12] M. Epstein, Buoyancy-driven exchange flow through small openings in horizontal partitions, *J. Heat Transf.* 110 (1988) 885–893.
- [13] Y. Jaluria, S.H.K. Lee, G.P. Mercier, Q. Tan, Transport processes across a horizontal vent due to density and pressure differences, *Exp. Therm. Fluid Sci.* 16 (1998) 260–273.
- [14] Y. Jaluria, W.K.S. Chiu, S.H.K. Lee, Flow of smoke and hot gases across horizontal vents in room fires, *Combust. Sci. Technol.* 110 (1995) 197–208.
- [15] Q. Tan, Y. Jaluria, Mass flow through a horizontal vent in an enclosure due to pressure and density differences, *Int. J. Heat Mass Transf.* 44 (2001) 1543–1553.
- [16] K. Venkatasubbaiah, Y. Jaluria, Numerical simulation of enclosure fires with horizontal vents, *Numer. Heat Transf. Part A* 62 (2012) 179–196.
- [17] W.K. Chow, Y. Gao, Buoyancy and inertial force on oscillations of thermal induced convective flow across a vent, *Build. Environ.* 46 (2011) 315–323.
- [18] W.K. Chow, Y. Gao, Oscillating behaviour of fire-induced air flow through a ceiling vent, *Appl. Therm. Eng.* 29 (2009) 3289–3298.
- [19] N.C. Markatos, K.A. Pericleous, Laminar and turbulent natural convection in an enclosed cavity, *Int. J. Heat Mass Transf.* 27 (1984) 755–772.
- [20] H. Chattopadhyay, K. Saha, Turbulent flow and heat transfer from a slot jet impinging on a moving plate, *Int. J. Heat Fluid Flow* 24 (2003) 859–868.
- [21] M.J. Cook, K.J. Lomas, Buoyancy-driven displacement ventilation flows: evaluation of two eddy viscosity models for prediction, *Build. Serv. Eng. Res. Technol.* 19 (1998) 15–21.
- [22] G.M. Stavrakakis, N.C. Markatos, Simulation of airflow in one- and two-room enclosures containing a fire source, *Int. J. Heat Mass Transf.* 52 (2009) 2690–2703.
- [23] A.H. Abib, Y. Jaluria, Turbulent penetrative and recirculating flow in a compartment fire, *J. Heat Transf.* 117 (1995) 927–935.
- [24] L. Davidson, Calculation of the turbulent buoyancy driven flow in a rectangular cavity using an efficient solver and two different low Reynolds number $k - \epsilon$ turbulence models, *Numer. Heat Transf. A* 18 (1990) 129–147.
- [25] A. Gupta, V. Eswaran, P. Munshi, N.K. Maheshwari, P.K. Vijayan, Thermal stratification studies in a side heated water pool for advanced heavy water reactor applications, *Heat Mass Transf.* 45 (2009) 275–285.
- [26] R. Harish, K. Venkatasubbaiah, Mathematical modeling and computation of fire induced turbulent flow in partial enclosures, *Appl. Math. Model.* 37 (2013) 9732–9746.
- [27] R. Harish, K. Venkatasubbaiah, Numerical simulation of turbulent plume spread in ceiling vented enclosure, *Eur. J. Mech. B Fluids* 42 (2013) 142–158.
- [28] V. Jan, M. Bart, D. Erik, Numerical study of natural convective heat transfer with large temperature differences, *Int. J. Numer. Method Heat Fluid Flow* 11 (2001) 329–341.
- [29] B. Roland, B. Malte, Solution of a stationary benchmark problem for natural convection with large temperature difference, *Int. J. Therm. Sci.* 41 (2002) 428–439.
- [30] P. Kumar, V. Eswaran, A numerical simulation of combined radiation and natural convection in a differential heated cubic cavity, *J. Heat Transf.* 132 (2010) 023501.
- [31] J. Ai, A.W.K. Law, S.C.M. Yu, On Boussinesq and non-Boussinesq starting forced plumes, *J. Fluid Mech.* 558 (2006) 357–386.
- [32] J.P. Abraham, E.M. Sparrow, Three-dimensional laminar and turbulent natural convection in a continuously discretely wall-heated enclosure containing a thermal load, *Numer. Heat Transf. A* 44 (2003) 105–125.
- [33] A. Demuren, H. Grotjans, Buoyancy driven flows—beyond the Boussinesq approximation, *Numer. Heat Transf. B* 56 (2009) 1–22.
- [34] R. Harish, K. Venkatasubbaiah, Numerical investigation of instability patterns and nonlinear buoyant exchange flow between enclosures by variable density approach, *Comput. Fluids* 96 (2014) 276–287.
- [35] Y.L. Chan, C.L. Tien, Numerical study of two-dimensional laminar natural convection in shallow open cavities, *Int. J. Heat Mass Transf.* 28 (1985) 612–630.
- [36] T.K. Sengupta, S.K. Sirkar, A. Dipankar, High accuracy schemes for DNS and acoustics, *J. Sci. Comput.* 26 (2006) 151–193.
- [37] H.N. Dixit, V. Babu, Simulation of high Rayleigh number natural convection in a square cavity using the lattice Boltzmann method, *Int. J. Heat Mass Transf.* 49 (2006) 727–739.
- [38] Y.S. Tian, T.G. Karayiannis, Low turbulence natural convection in an air filled square cavity part I: the thermal and fluid flow fields, *Int. J. Heat Mass Transf.* 43 (2000) 849–866.